

ARTICLE OPEN

Electride and superconductivity behaviors in Mn_5Si_3 -type intermetallicsYaoqing Zhang^{1,2}, Bosen Wang³, Zewen Xiao^{1,2}, Yangfan Lu^{1,2}, Toshio Kamiya², Yoshiya Uwatoko³, Hiroshi Kageyama⁴ and Hideo Hosono^{1,2}

Electrides are unique in the sense that they contain localized anionic electrons in the interstitial regions. Yet they exist with a diversity of chemical compositions, especially under extreme conditions, implying generalized underlying principles for their existence. What is rarely observed is the combination of electride state and superconductivity within the same material, but such behavior would open up a new category of superconductors. Here, we report a hexagonal Nb_5Ir_3 phase of Mn_5Si_3 -type structure that falls into this category and extends the electride concept into intermetallics. The confined electrons in the one-dimensional cavities are reflected by the characteristic channel bands in the electronic structure. Filling these free spaces with foreign oxygen atoms serves to engineer the band topology and increase the superconducting transition temperature to 10.5 K in Nb_5Ir_3O . Specific heat analysis indicates the appearance of low-lying phonons and two-gap *s*-wave superconductivity. Strong electron–phonon coupling is revealed to be the pairing glue with an anomalously large ratio between the superconducting gap Δ_0 and T_c , $2\Delta_0/k_B T_c = 6.12$. The general rule governing the formation of electrides concerns the structural stability against the cation filling/extraction in the channel site.

npj Quantum Materials (2017)2:45; doi:10.1038/s41535-017-0053-4

INTRODUCTION

Superconductivity energy gap opens when the Cooper pairs are condensed into a coherent ground state. The microscopic mechanism sustaining such pairing of electrons typically involves electron–phonon coupling as the glue, but in unconventional cases magnetic excitations and other delicately balanced factors may dominate.^{1–3} A consequence of the complexity is that discovering new superconducting materials largely remains a rather haphazard process.^{4–6} Our favored approach is to examine a group of uniquely structured compounds in which the crystallographic cavity space confines excess electrons rendering them an anionic nature. Conceptually, we describe these materials as electrides.^{1, 7–12} A canonical example is the completely reduced mayenite, $[Ca_{12}Al_{14}O_{32}]^{2+} \cdot 2e^-$ which exhibits remarkably rich chemistries.^{13–16} Of particular note is the observation of a superconducting transition ($T_c \sim 0.4$ K) intimately related to the anionic electrons in this electride, thereby opening a new frontier in the field of superconductors.¹⁷

The range of electrides has been extended from cage structured mayenite to both layered and one-dimensional (1D) types. Compared to the strongly reactive layered electrides, such as $[Ca_2N]^+ \cdot e^-$ and $[Y_2C]^{1.8+} \cdot 1.8e^-$, the air stable 1D analogues promise a more friendly system to work on.^{18–21} From a structural perspective, the topology of the cation arrays in our 1D apatite electride $[La_8Sr_2Si_6O_{24}]^{4+} \cdot 4e^-$ approximates that of the Mn_5Si_3 structure which hosts another 1D electride Y_5Si_3 .^{20, 21} The presence of anionic electrons is associated with the formation of new energy states near the Fermi level with weak

electron–phonon interaction, which is indicative of a good source for superconductivity. We are, therefore, motivated to look for possible combined electride and superconducting states by further exploring the chemical variety of Mn_5Si_3 -type A_5B_3 phases (A: rare earth or transition metals; B: Ga, Si, Ge, etc).

Crystallizing in hexagonal symmetry (space group $P6_3/mcm$), the Mn_5Si_3 unit cell is characterized by three distinct crystallographic sites, Si, Mn(I) and Mn(II), see Fig. 1a, b. The Si atoms generate a network of twisted trigonal prisms so as to accommodate Mn(I) atoms in the center. Such slightly distorted prisms are linked by planes down the *c*-axis stacking direction forming a linear Mn(I) skewer structure. The in-plane edge sharing gives rise to a zeolitic framework to accommodate an octahedral array of remaining Mn(II) atoms. Like in many chalcogenides and halides of the 4*d* and 5*d* transition elements,²² all like octahedral units here are interconnected forming infinite $[Mn_3]$ channels along the $[001]$ direction. In fact, such structures have been considered to be favorable to superconductivity as in A15-type superconducting phases.²³ As an example, a recent study has claimed the first superconductor Zr_5Sb_3 with $T_c \sim 2.3$ K within this structural domain.²⁴

In this work, the isostructural Nb_5Ir_3 attracts our attention in consideration of the superconducting nature of the Nb element and sporadic reports on the superconducting behavior of the binary Nb–Ir phases.^{25–27} In virtue of the experiments and theoretical calculations, we find that the phase diagram for Nb–Ir hosts a hexagonal phase with interesting interplay of superconductivity and electride state. The characteristic band structure can be engineered via introduction of guest atoms into

¹ACCEL Project, Japan Science and Technology Agency (JST), Tokyo 102-8666, Japan; ²Materials Research Center for Element Strategy, Tokyo Institute of Technology, Yokohama 226-8503, Japan; ³Institute for Solid State Physics, University of Tokyo, Kashiwa 277-8581, Japan and ⁴Department of Energy & Hydrocarbon Chemistry, Kyoto University, Kyoto 615-8510, Japan

Correspondence: Yaoqing Zhang (yaoqing.zhang@gmail.com) or Hideo Hosono (hosono@mssl.titech.ac.jp)
Yaoqing Zhang, Bosen Wang and Zewen Xiao contributed equally to this work

Received: 23 March 2017 Revised: 14 July 2017 Accepted: 18 July 2017

Published online: 15 August 2017

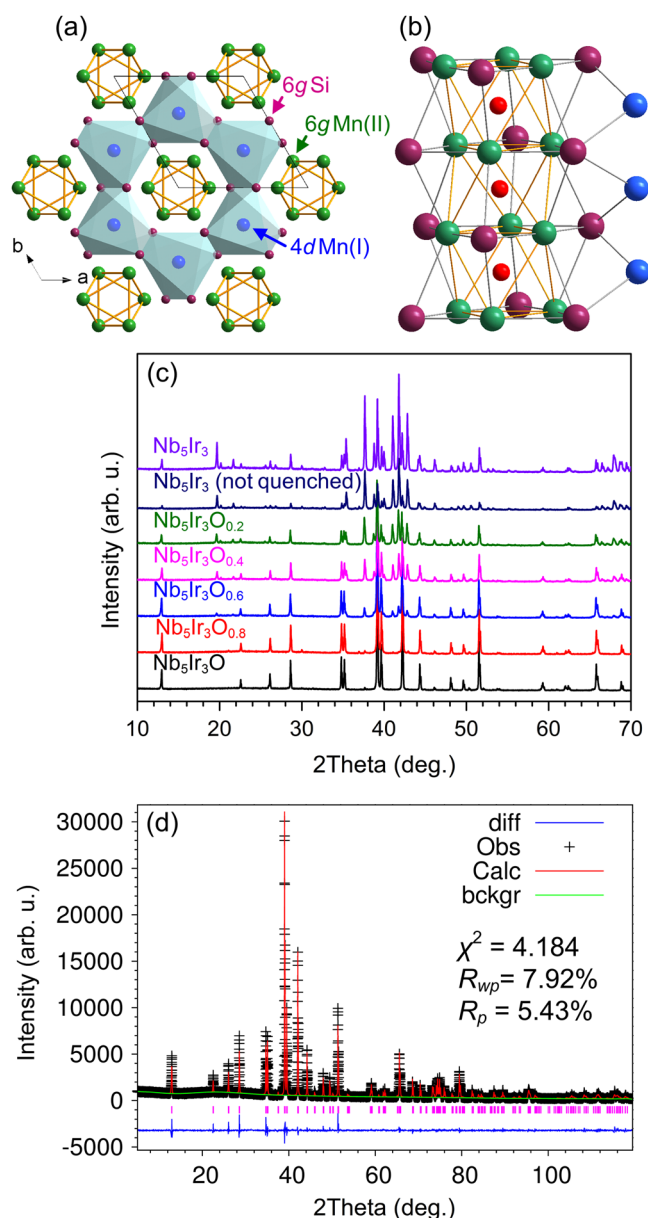


Fig. 1 An illustration of the Mn₅Si₃-type crystal structure and x-ray diffraction patterns for Nb₅Ir₃. **a** Shaded polyhedral Si (the plum spheres) complexes are twisted Si₆ trigonal prisms which accommodate Mn(II) atoms (the blue spheres) in the centre. **b** The 6g Mn(II) atoms (the green spheres) form chains of confacial trigonal antiprisms in which the channel space can be filled by guest atoms (the red spheres), while the 4d Mn(I) atoms construct another linear structure. **c** XRD patterns collected on a series of Nb₅Ir₃O_x (0 ≤ x ≤ 1) phases quenched in liquid nitrogen unless specified. **d** A Rietveld refinement analysis of data for single-phased Nb₅Ir₃O

the cavity sites for targeted properties, showing a rather intriguing base for the development of intrinsic, stable and functional electrides.

RESULTS

Synthesis and band structures

Our consideration is to synthesize all-transition-metal variants for electron-enriched compounds. With Nb and Ir as the chemical pair, a solid state reaction of element powders in a molar ratio of

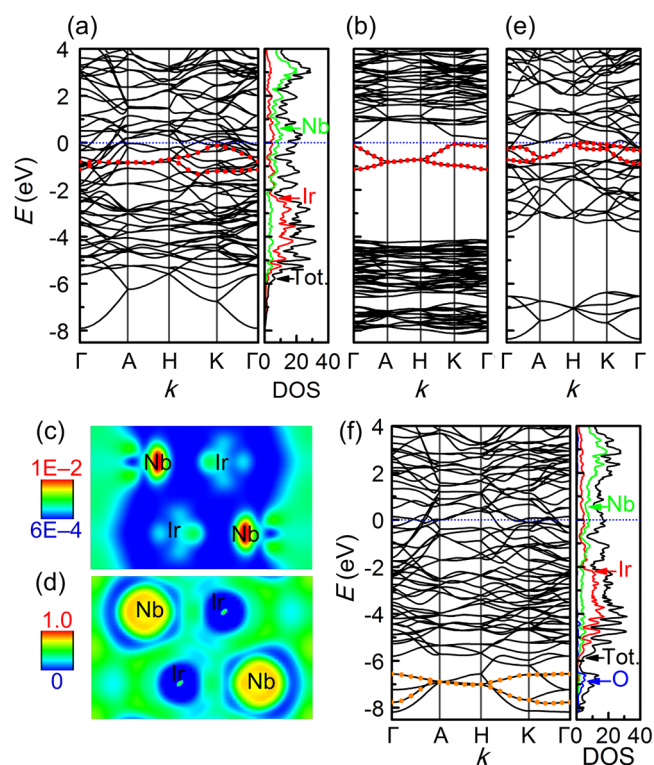


Fig. 2 Electronic structures of different materials. Calculated band structures and density of states (DOS) for **a** [Nb₅Ir₃]²⁺·2e⁻ with corresponding electron density for the channel bands (ChBs) and electron localization function (ELF) map on the (1–100) plane parallel to the *c*-axis in **c** and **d**, respectively, and **f** Nb₅Ir₃O. **b**, **e** Band structures of one-dimensional (1D) electrides **b** [La₈Sr₂(SiO₄)₆]¹⁴⁺·4e⁻ and **e** Y₅Si₃. The characteristic ChBs are circled in red for all electrides

5:3 by heating at 1200 °C in an evacuated silica jacket yielded air stable black products. X-ray diffraction (XRD) analysis shows that the obtained samples crystallize as a mixture of tetragonal and hexagonal phases. As shown in Fig. 1c, the diffraction peaks of the XRD pattern for Nb₅Ir₃ can be indexed into a Mn₅Si₃-type unit cell (*a* = 7.858(4) Å, *c* = 5.101(3) Å, space group: *P6₃/mcm*) and a second phase with a tetragonal structure (*a* = 9.841(3) Å, *c* = 5.069(3) Å, space group: *P4₂/m*). The former hexagonal phase of Nb₅Ir₃ receives little attention in the literature. In contrast, the latter tetragonal symmetry belongs to the σ phase and has been extensively studied concerning superconductivity. Synthesizing monophasic Nb₅Ir₃ proved to be challenging, nevertheless, upon quenching in liquid nitrogen, the concentration of the hexagonal phase increases (Fig. 2c), indicating the possibility to stabilize the hexagonal structure at ambient conditions. A Rietveld refinement analysis suggests a ratio of 60.8:39.2 between the hexagonal and tetragonal phases, see Supplementary Fig. 1. Introducing stabilizing oxygen atoms into the octahedral voids indeed enables pure hexagonal phases and we shall discuss the details later.

At first, we show the calculated band structures of Nb₅Ir₃, Nb₅Ir₃O, and relevant electride materials for insight into the electron states by using density functional theory (DFT). From Fig. 2a, Nb₅Ir₃ is found to be a multiband metal with the states at the Fermi level mainly consisting of Nb 4*d* and Ir 5*d* orbitals. More interestingly, in analogy to the known 1D apatite electride [La₈Sr₂(SiO₄)₆]¹⁴⁺·4e⁻ where four anionic electrons occupy two channel bands (ChBs) as in Fig. 2b, Nb₅Ir₃ shows two similar ChBs just below the Fermi level (marked by red circles in Fig. 2a), which are associated with the two interstitial sites, i.e., at (0, 0, 0) and (0, 0, 1/2), in the channel space. These two ChBs are localized along

the direction perpendicular to the channels (e.g., the A–H direction), but delocalized along the channel directions (e.g., the H–K direction), implying that the ChBs states are confined within the 1D channel space, similar to the 1D apatite electride [La₈Sr₂(SiO₄)₆]⁴⁺·4e⁻.²⁰ A further examination of the ChBs-associated electron density (Fig. 2c) and electron localization function (Fig. 2d) confirms that the confinement of ChBs electrons in the channel with ionic bonding to the [Nb₅Ir₃]²⁺ framework. As a result, we are able to conclude that Nb₅Ir₃ is an intermetallic electride with a [Nb₅Ir₃]²⁺·2e⁻ configuration. For a simple comparison, we revisited the recently reported isostructural Y₅Si₃ electride and confirmed the existence of two similar characteristic ChBs (i.e., the two bands *red circled* in Fig. 2e). On the other hand, it is found that the oxygen-containing Nb₅Ir₃O presents a very different band structure, as the ChBs are now far away from the Fermi level, which may be evidence for the disappearing electride property. In the following text, both Nb₅Ir₃ and Nb₅Ir₃O are revealed to be superconducting with relative high T_c . It is to say that Nb₅Ir₃ exhibits both electride and superconducting behaviors, whereas only superconductivity remains in Nb₅Ir₃O. The finding on the combination of electride and superconductivity is quite unusual and we set a record for the transition temperature for this category of superconductors.

Superconducting properties

Shown in Supplementary Fig. 2a is the temperature dependence of resistivity under zero magnetic field. The hexagonal Nb₅Ir₃ shows a metallic behavior on cooling. Resistivity drops abruptly at a critical temperature $T_{c1}^{\text{onset}} \sim 9.4$ K, and down further until zero at $T_{c2}^{\text{onset}} \sim 2.8$ K, suggestive of the two coexisting superconducting phases. Here, T_c^{onset} is defined as the temperature at which the resistivity begins to decrease. The temperature dependence of susceptibility of quenched Nb₅Ir₃ at a magnetic field of 10 Oe is shown in Supplementary Fig. 2b, consistent with the resistivity data. Around T_{c1}^{onset} , the transition is sharp with a transition width of ~ 0.5 K in both resistivity and susceptibility. The pronounced hysteresis between magnetization curves on zero-field cooled and field cooled substantiates a type-II superconductivity. Thus, the two phases of Nb₅Ir₃ are both superconductors. Meanwhile, the low-temperature superconductivity is found to vanish gradually when the tetragonal phase diminishes from the XRD patterns; consistent with previous findings.²⁷ This is illustrative of their competing relationship. Thus, the higher T_c is from hexagonal Nb₅Ir₃ while tetragonal Nb₅Ir₃ shows the lower T_c . In other words, hexagonal Nb₅Ir₃ is not only an intermetallic electride, but actually a superconductor with a transition temperature much higher than that of the first superconducting electride [Ca₁₂Al₁₄O₃₂]²⁺·2e⁻ ($T_c \sim 0.4$ K).

Compared to the known Mn₅Si₃-type superconductors, Nb₅Ir₃ exhibits the highest T_c . However, the presence of the competing tetragonal phase necessitates an optimized synthesis for a pure phase. In many cases, Mn₅Si₃-type materials have to bind interstitial atoms to stabilize the host structure.^{28–30} For the current composition, Horyn and co-worker³¹ have tried to incorporate interstitial oxygen atoms, showing that the resultant compound remains superconductive; the superconducting mechanism was however not discussed. Using Nb₂O₃ as the oxygen source, we prepared a series of Nb₅Ir₃O_x samples with $0 \leq x \leq 1$. As evidenced in Fig. 1c, with growing oxygen concentration, the tetragonal phase is increasingly suppressed, whereas the hexagonal structure becomes more dominant. At a nominal composition of Nb₅Ir₃O, a single-phased Mn₅Si₃-type structure is formed. A Rietveld refinement of the XRD profile, see Fig. 1d, reveals that the oxygen occupies the channel cavity sites (0, 0, 0) and (0, 0, 1/2), in consistency with previous studies on the isostructural compounds.^{28–30} The almost linear change of unit cell parameters as a function of oxygen content in Nb₅Ir₃O_x further

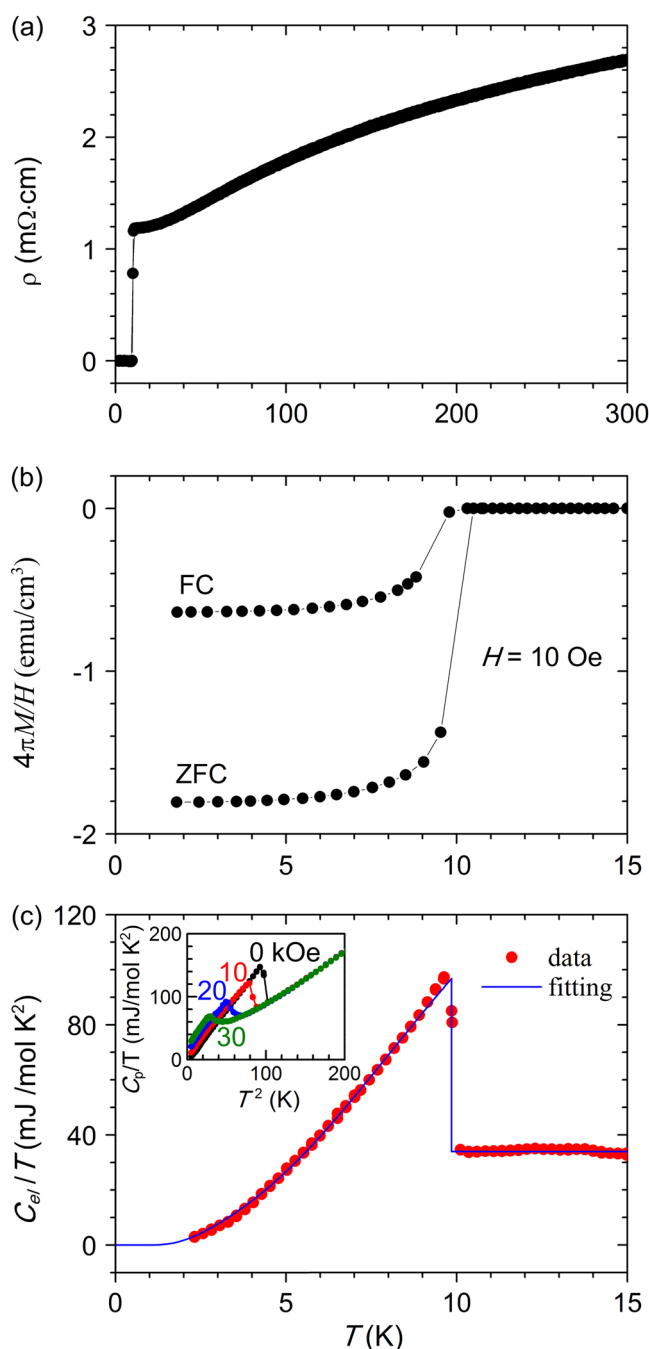


Fig. 3 Evidence for bulk superconductivity in Nb₅Ir₃O. **a** Temperature-dependent resistivity at zero magnetic field. **b** Magnetic susceptibility curve under an applied field of $H = 10$ Oe. **c** The electronic contribution to specific heat fitted according to a two-gap model. Inset is the specific heat measurement with and without magnetic field

substantiates the insertion of oxygen into the vacant lattice sites (Supplementary Fig. 3). The Nb–O interatomic distance is 2.28 Å, indicative of the bond formation. The Nb1 atoms define a linear chain with a short Nb–Nb interatomic distance of $c/2 \sim 2.55$ Å compared with ~ 2.99 Å separations in face centered cubic Nb.³² This chain of very closely spaced transition metals is a notable feature of the present crystal structure. The Nb2 atoms are more loosely packed in the octahedral units with the Nb–Nb distance

between 3.17 and 3.28 Å. In other words, the relatively weak Nb₂–Nb₂ bonding in Nb₅Ir₃ is converted to Nb–O bonding in Nb₅Ir₃O.

Subsequent characterizations of the superconducting property of the stabilized hexagonal Nb₅Ir₃O were carried out. Figure 3a shows the temperature dependence of resistivity and susceptibility. Resistivity decreases sharply to zero at an onset temperature ~10.5 K. Susceptibility as a function of temperature was measured at 10 Oe in Fig. 3b. A sharp drop indicating the superconductivity appears at around 10.5 K, which is in excellent agreement with the zero resistivity temperature. For the merit of discussion hereafter, we define the onset temperature as the superconducting temperature for both Nb₅Ir₃ and its derivative Nb₅Ir₃O. The nature of superconductivity is supported by the presence of a large anomalous jump in the specific heat, which also signals a homogeneous sample. As can be seen from Fig. 3c inset, as the magnetic field increases, the jump was gradually suppressed and shifted toward a lower temperature. Also, the superconducting transition is found to broaden with increasing magnetic field (Fig. 3c and inset), indicating strong magnetic pinning effect as revealed in many known type-II superconductors.

To extract more information, the specific heat at the normal state $C_N(T)$ was firstly estimated from the data under 5 T. As in Supplementary Figure 4, $C_N(T)/T$ departs from a linear dependence on T^2 , suggesting the existence of low-lying phonons. Accordingly, $C_N(T)$ was fitted based on the function $C_N(T) = \gamma T + \beta T^3 + \delta T^5$ where the first and latter two terms represent the contributions from electrons and phonons, respectively. The obtained parameters are $\gamma = 33.89 \text{ mJ mol}^{-1} \text{ K}^{-2}$, $\beta = 0.40963 \text{ mJ mol}^{-1} \text{ K}^{-4}$ and $\delta = 1.413 \times 10^{-3} \text{ mJ/mol K}^6$. The specific heat jump at T_c , $\Delta C/\gamma T_c$, is approximately 1.86, notably larger than the expected value of 1.43 for a typical BCS (Bardeen–Cooper–Schrieffer) superconductor with a weak coupling limit, indicative of a strong electron–phonon coupling that serves as the glue of Cooper pairs in this system.³³ The Debye temperature is estimated to be $\theta_D = 350 \text{ K}$, using the relationship $\beta = (12\pi^4/5)N R/\theta_D^3$, where N is the atom number in a formula unit and R is the gas constant. From the McMillan formula,³⁴ $T_c = (\theta_D/1.45) \exp[-1.04(1 + \lambda_{ph})/(\lambda_{ph} - \mu^*(1 + 0.62 \lambda_{ph}))]$, together with the assumption of the Coulomb pseudopotential $\mu^* = 0.15$,³⁵ the electron–phonon coupling constant was estimated to be $\lambda_{ph} = 0.82$, indicating a strongly coupled superconductor, similar to LaMo₆S₈ with $\lambda_{ph} = 0.85$.³⁶ In Fig. 3c, the electronic contribution $C_{el}(T)$ to specific heat is extracted by subtracting the lattice contribution $C_N(T)$ from the total. We find that neither a simple BCS weak-coupling limit nor a single gap α model could reproduce the data in Fig. 3c. It implies that $C_{el}(T)$ below T_c behaves like a strong coupling superconductivity with a finite energy gap. A quantitative analysis of $C_{el}(T)$ by employing the two-gap model leads to a perfect fitting (Fig. 3c), yielding $a_1 = 1.14$ and $a_2 = 3.06$, indicating that two superconducting energy gaps of an *s*-wave symmetry with the different size develop simultaneously at T_c . The larger gap corresponding to the electron states strongly coupled to phonons is believed to be dominant in the superconductivity. The derived $2\Delta_0/k_B T_c$ of ~6.12 far exceeded the weak coupling BCS value 3.52. Such a strong coupling superconductivity is relatively rare, but comparable to Pb–Bi alloy, pyrochlore osmates and SrPt₃P.^{37–39} Also, we have noticed evidence of strong coupling of electrons with low-lying phonons in resistivity as shown in Fig. 3a. Above 100 K, the resistivity becomes increasingly saturated because the electron mean free path becomes essentially close to the atomic lattice spacing. Such resistivity saturation has been observed in other strong coupling superconductors and it is usually seen as evidence for strong coupling between electrons and low-lying phonons.³⁹ Thus, the above results indicate that Nb₅Ir₃O is a two-gapped *s*-wave, strongly coupled superconductor.

The Wilson ratio R_w was also determined based on $R_w = \pi^2 k_B^2 \chi_0 / 3\mu_B^2 \gamma$ where k_B is the Bohr magneton.⁴⁰ The magnetic

susceptibility in the normal state (Supplementary Fig. 5) can be fitted to the formula $\chi = \chi_0 + C_w/(T - \theta)$, where χ_0 is a temperature-independent term, C_w is the Curie–Weiss constant, and θ is the Weiss temperature. The fitting yields $\chi_0 = 4.09 \times 10^{-4} \text{ emu mol}^{-1}$, $C_w = 1.04 \times 10^{-3} \text{ emu K mol}^{-1}$ and $\theta = -6.2 \text{ K}$. Assuming the orbital susceptibility is negligible, that is to use the obtained χ_0 as spin susceptibility, we acquire $R_w = 0.81$, a value that tends to be overestimated due to the non-negligible spin-orbit interaction, but is in full support of the strong electron–phonon coupling.

Assuming most Cooper pairs are broken at T_c , we can plot the upper critical field $H_{c2}(T)$ from the ρ data under various magnetic fields (Supplementary Fig. 6a). As shown in Supplementary Figure 6b, by using the Ginzburg–Landau (GL) equation $H_{c2}(T) = H_{c2}(0) \times (1 - t^2)/(1 + t^2)$, where the reduced temperature $t = T/T_c$, the experimental data were fitted generating a ground state value $H_{c2}(0) = 11.6 \pm 0.6 \text{ T}$. According to the GL theory,³⁰ the H_{c2} value is related to the GL coherent length (ξ_{GL}) in the form of $H_{c2} = \varphi_0 / 2\pi \xi_{GL}^2$ (φ_0 being the magnetic quantum). From this formula, $\xi_{GL} = 5.33 \text{ nm}$ can be obtained. The lower critical field H_{c1} , extracted from the magnetic field (Supplementary Figure 6c) where the magnetization curve departs from the linear response, was plotted in Supplementary Figure 6d. Applying the empirical function $H_{c1}(T) = H_{c1}[1 - a(T/T_c)^2]$ (a is a fitting parameter) gives rise to $H_{c1}(0) = 147 \pm 5 \text{ Oe}$. The London penetration depth (λ) derived from the BCS formula $H_{c2}/H_{c1} = 2\kappa^2 \ln \kappa$ with $\kappa = \lambda/\xi$ is 201 nm, while the GL parameter (κ) is 37.87.

Properties under high pressure

To reveal more details with respect to the pairing mechanism, a study under pressure was further conducted. Combining resistivity and magnetization results in Supplementary Fig. 7 gives the pressure dependence of T_c^M and T_c^{zero} which are referred to as the temperatures where diamagnetism appears and resistivity

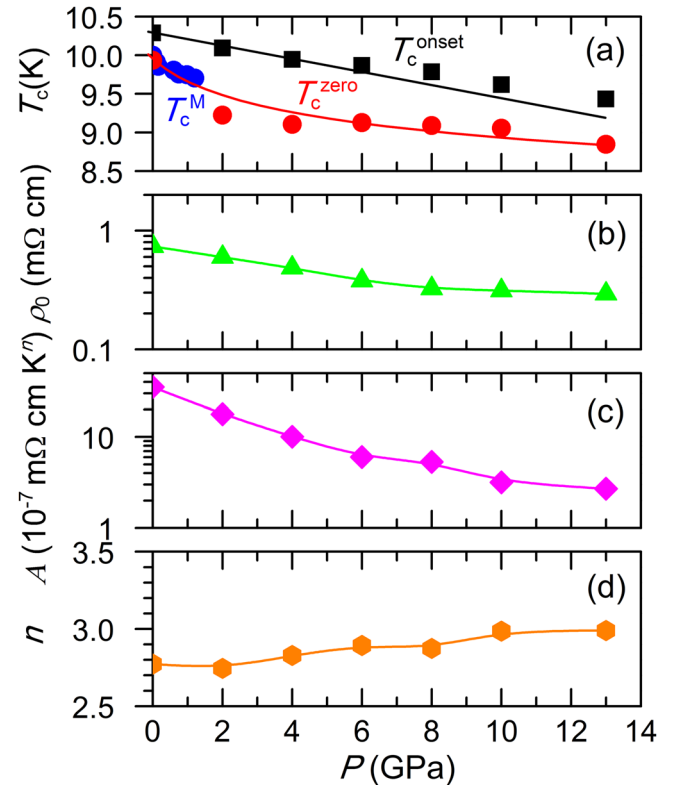


Fig. 4 Measured transport parameters under pressure. Pressure (P) dependence of superconducting transition temperature **a**, and resistivity fitting parameters, ρ_0 and n **b–d**

becomes zero, respectively, see Fig. 4a. While both temperatures are closely related, it is noted T_c^{onset} decreases monotonically from 10.1 K at ambient pressure to 9.2 K at 8 GPa. A linear fitting in the range of $0.1 \text{ MPa} < P < 13 \text{ GPa}$ yields a negative differential pressure coefficient of -0.08 K GPa^{-1} . An analysis of the normal-state resistivity (ρ) just above T_c was performed through a fitting against the residual resistivity ρ_0 , coefficient A and the exponent n based on the function $\rho = \rho_0 + AT^n$, see Supplementary Fig. 8. The estimated parameters were shown in Fig. 4b–d. It can be seen that both T_c^{onset} and T_c^{zero} show the same trend in the whole pressure range. At ambient pressure n is nearly 2.5, and it increases gradually up to 3 above 10 GPa. The derived n is much smaller than the typical value ($n=5$) for an electron–phonon scattering dominated case, consistent with strong-coupling superconductivity. The ρ_0 is found to decrease under pressure due to the polycrystalline nature of the sample. The inelastic scattering term A can serve as a measure of $N(E_F)$. Hence, the smaller A under pressure (nearly one order of magnitude decrease) is related to the reduced $N(E_F)$ due to the renormalized wide bandwidth. The reduced T_c under pressure is expected resulting from the decreasing density of states (DOS) at the Fermi level associated with the increased orbital hybridizations. But, it is unusual that the pressure coefficient is notably smaller than that of other traditional BCS superconductors such as metals, indicating some other interactions or correlations are in favor of the superconducting state. As one example, the introduction of Ir atoms or Ir–Nb bonds in an itinerant electronic superconductor may provide some local magnetic moments, and their interplay has been revealed to play a critical role in unconventional superconductivity. This implies a unique superconducting state in Nb₅Ir₃O. One may also consider the pressure effect is due to the depression of electrone, i.e. the electron concentration at interstitial sites, which shifts electrons to d orbitals of Nb and Ir. This would serve to further increase the DOS at Fermi level which will in turn favor the superconductivity, although overall T_c decreases.

DISCUSSION

Now we consider the enhanced T_c of Nb₅Ir₃O compared to the parent Nb₅Ir₃. From Supplementary Fig. 9, the major variable that affects the superconductivity seems to be the amount of O because T_c is enhanced as a generally linear response to increasing oxygen content. This is in stark contrast to the case of Zr₅Sb₃ in which filling the same channel sites with guest atoms, e.g. C, O and Sb, would suppress the superconductivity.²⁴ We may link such an increase to the crystal chemistry of Nb₅Ir₃O. Upon binding O, the principal dimensional change taking place is the contraction of all cells down the c -axis, though the cell is expanded along the (001) plane (Supplementary Fig. 3). This means the octahedral chains along the c -axis become increasingly distorted when Nb–O bonds are formed. As in a similar interstitial filled Sb₅RE₃Ti (RE: rare earth),⁴¹ the position of the Fermi level is quite sensitive to even minor changes that lead to small contractions in the structure. Ir is the most electronegative component among these metal elements and, therefore, the Zintl concept may be applicable by assuming that a full electron transfer takes place. Hence, the Nb atom donates its valence electrons to both oxygen and iridium atoms whereas the remaining electrons are utilized to form a single pair bond with a neighboring metal atom. In this sense, we may expect O $2p$ and Nb $4d$ will contribute extra states to the energy region that hosts the Fermi level, while the σ -overlap of Nb dz^2 orbitals within the linear Nb skewers still plays a dominating role. The larger DOS at Fermi level or γ value in Nb₅Ir₃O should account for the higher T_c . In support of this scenario, a smaller γ value ($24.1 \text{ mJ mol}^{-1} \text{ K}^{-2}$) in Zr₅Sb₃ has been reported with a lower T_c . On the other hand, as can be found in calculations, inserting O atoms can push the ChBs

down to approximately 6 eV below Fermi level, yet the transition temperature increases. Another likely reason is the involvement of O phonon modes that may have a higher frequency and stronger coupling to electrons close to the Fermi level.

As for electrone, while the apatite structured [La₈Sr₂(SiO₄)₆]¹⁴⁺:4e[−] has to be prepared by extracting two channel oxygens from La₈Sr₂(SiO₄)₆O₂, Nb₅Ir₃ is an intrinsic one with open channel spaces. When the two channel sites are completely filled by oxygen, Nb₅Ir₃O is formed. Figure 2f shows the band structure and DOS for Nb₅Ir₃O. It can be observed that the loosely bound ChBs states (right below the Fermi level) for Nb₅Ir₃ are transferred to oxygen to form oxide anions. The resulting tightly bound O $2p^6$ states are pushed down into a much deeper energy level. Interestingly, among the six O $2p$ bands, two of them (orange circled in Fig. 2f) retain the dispersion character of the ChBs in 1D electrone. Therefore, in general, the ChBs correspond to the channel sites directly and their energy levels rely on binding force of the anions. When the channel structure is open, the ChBs states are loosely bound and serve as anions themselves. To take one step further, electrone can be viewed to be intimately related to materials that are amenable to cation filling but undergo no structural degradations. This general rule may serve as the fundamental tenet for the electrone development and define a direction towards more superconducting electrone.

To summarize, we have demonstrated an entirely new intermetallic electrone with electrons detached from the lattice framework atoms but localized in the 1D channel space. This electrone is also a superconductor below a critical transition temperature of $T_c = 9.4 \text{ K}$. The superconducting behavior is tunable by controlling the ChBs arising from the electrons that are responsible for the electrone state. Filling the free spaces with interstitial oxygen not only stabilizes the host hexagonal lattice, but also helps to engineering the band topology. As a result, the superconducting transition temperature (T_c) was increased up to 10.5 K in Nb₅Ir₃O. Such a T_c enhancement is in distinct contrast to the case of Zr₅Sb₃ whose superconducting state is subject to suppression upon binding any guest species. Specific heat analysis indicates the appearance of low-lying phonons and two-gap s -wave superconductivity. Strong electron–phonon coupling is revealed to be the pairing glue with an anomalously large ratio between the superconducting gap Δ_0 and T_c , $2\Delta_0/k_B T_c = 6.12$. Under pressure, the decreasing DOS at the Fermi level associated with the increased orbital hybridizations leads to decreased T_c . We also show a general rule for the formation of electrone which is closely related to the structural stability against the cation filling/extraction in the channel site, suggesting a new avenue towards the discovery of more electrone materials.

METHODS

Materials synthesis

Polycrystalline samples of Nb₅Ir₃ and Nb₅Ir₃O_{*x*} were synthesized by the solid state reaction. Stoichiometric amounts of Nb, Ir and Nb₂O₃ precursor powders were mixed and pressed into pellets before sealed in a quartz tube under vacuum of around 10^{-3} mbar. The reaction was at 1200 °C for 72 h followed by a quenching process in either air or liquid nitrogen.

Characterizations

The purity of the precursors and the products was checked by XRD using a D8 ADVANCE diffractometer with Cu K_α radiation. Structural parameters were generated from Rietveld refinement using GSAS software with EXPGUI interface.^{42, 43} Magnetic susceptibilities of all samples were measured by a superconducting quantum interface device magnetometer (SQUID) in the temperature range of 2–300 K under applied external magnetic fields. The electrical resistivity and the specific heat under the ambient pressure were measured above 1.8 K by using the commercial Physical Properties Measurement System (MPMS). The resistivity under high pressure was measured by using a cubic anvil apparatus, which

generated quasi-hydrostatic pressures up to 8 GPa. A preheated pyrophyllite cube was used as the gasket and the glycerol was used as the pressure transmitting medium. Each measurement was carried out at a fixed pressure on warming process.

DFT Calculations

DFT calculations were performed for Nb₅Ir₃ and Nb₅Ir₃O together with two reported 1D electrides [La₈Sr₂(SiO₄)₆]⁴⁺·4e⁻ and Y₅Si₃ using the generalized gradient approximation (GGA) with the Perdew–Burke–Ernzerhof (PBE)⁴⁴ functional and the projector augmented plane-wave method as implemented in the VASP code.⁴⁵ The plane wave cutoff energy was set to 500.0 eV. A 6 × 6 × 10 *Γ*-centered *k*-mesh was used to sample the first Brillouin zone. Prior to the electronic structure calculations, the crystal structures were fully relaxed and considered to be converged when the total force on each atom was less than 0.01 eV/Å.

Data availability

The data that support the findings of this study are available in the article and [Supplementary Information](#).

ACKNOWLEDGEMENTS

H.H. is indebted to the support by the Japan Society for the Promotion of Science (JSPS) through a Grant-in-Aid for Scientific Research (S) No.17H06153. Dr. Y. Kobayashi in Kyoto University is gratefully acknowledged for the fruitful discussions on the Rietveld refinement. We thank Prof J. G. Cheng in the Institute of Physics, CAS and Prof. K. Matsubayashi in University of Electro-Communications for their comments on the manuscript. We thank S. Nagasaki in the Institute for Solid State Physics, University of Tokyo for technical assistance during the high pressure measurements.

AUTHOR CONTRIBUTIONS

Y.Z. conceived the idea, synthesized the samples and measured X-ray diffraction and physical properties. B.W. collected and analyzed high pressure results. Z.X. performed the theoretical calculations and contributed to data discussion. Y.L. measured and analyzed heat capacity data. Y.Z. wrote the manuscript with contributions from B.W. and Z.X. T.K., Y.U. and H.K. commented on the manuscript. H.H. supervised the project.

ADDITIONAL INFORMATION

Supplementary Information accompanies the paper on the *npj Quantum Materials* website (doi:[10.1038/s41535-017-0053-4](https://doi.org/10.1038/s41535-017-0053-4)).

Competing Interests: The authors declare that they have no competing financial interests.

Publisher's note: Springer Nature remains neutral with regard to jurisdictional claims in published maps and institutional affiliations.

REFERENCES

- Cooper, L. N. & Feldman, D. E. *BCS: 50 Years*. (World Scientific, 2011).
- Cava, R. J. Oxide superconductors. *J. Am. Ceram. Soc.* **83**, 5–28 (2000).
- Wang, F. & Lee, D.-H. The electron-pairing mechanism of iron-based superconductors. *Science* **332**, 200–204 (2011).
- Bednorz, J. G. & Müller, K. A. Possible high *T_c* superconductivity in the BaLaCuO system. *Z. Phys. B* **64**, 189–193 (1986).
- Kamihara, Y., Watanabe, T., Hirano, M. & Hosono, H. Iron-based layered superconductor La[O_{1-x}F_x]FeAs (*x* = 0.05–0.12) with *T_c* = 26 K. *J. Am. Chem. Soc.* **130**, 3296–3297 (2008).
- Hosono, H. Layered iron pnictide superconductors: discovery and current status. *J. Phys. Soc. Jpn* **77**, 1–8 (2008).
- Dye, J. L. Electrides: ionic salts with electrons as the anions. *Science* **247**, 663–668 (1990).
- Ma, Y. et al. Transparent dense sodium. *Nature* **458**, 182–185 (2009).
- Pickard, C. J. & Needs, R. J. Dense low-coordination phases of lithium. *Phys. Rev. Lett.* **102**, 146401 (2009).
- Marqués, M. et al. Potassium under pressure: a pseudobinary ionic compound. *Phys. Rev. Lett.* **103**, 115501 (2009).

- Miao, M.-S. & Hoffmann, R. High pressure electrides: a predictive chemical and physical theory. *Acc. Chem. Res.* **47**, 1311–1317 (2014).
- Miao, M.-S. & Hoffmann, R. High-pressure electrides: the chemical nature of interstitial quasisatoms. *J. Am. Chem. Soc.* **137**, 3631–3637 (2015).
- Matsuishi, S. High-density electron anions in a nanoporous single crystal: [Ca₂₄Al₂₈O₆₄]⁴⁺(4e⁻). *Science* **301**, 626–629 (2003).
- Kim, S. W., Shimoyama, T. & Hosono, H. Solvated electrons in high-temperature Melts and glasses of the room-temperature stable electride [Ca₂₄Al₂₈O₆₄]⁴⁺·4e⁻. *Science* **333**, 71–74 (2011).
- Toda, Y. et al. Work function of a room-temperature, stable electride [Ca₂₄Al₂₈O₆₄]⁴⁺(e⁻)₄. *Adv. Mater.* **19**, 3564–3569 (2007).
- Kitano, M. et al. Ammonia synthesis using a stable electride as an electron donor and reversible hydrogen store. *Nat. Chem.* **4**, 934–940 (2012).
- Miyakawa, M. et al. Superconductivity in an inorganic electride 12CaO·7Al₂O₃·e⁻. *J. Am. Chem. Soc.* **129**, 7270–7271 (2007).
- Lee, K., Kim, S. W., Toda, Y., Matsuishi, S. & Hosono, H. Dicalcium nitride as a two-dimensional electride with an anionic electron layer. *Nature* **494**, 336–340 (2013).
- Zhang, X. et al. Two-dimensional transition-metal electride Y₂C. *Chem. Mater.* **26**, 6638–6643 (2014).
- Zhang, Y., Xiao, Z., Kamiya, T. & Hosono, H. Electron confinement in channel spaces for one-dimensional electride. *J. Phys. Chem. Lett.* **6**, 4966–4971 (2015).
- Lu, Y. et al. Water durable electride Y₅Si₃: electronic structure and catalytic activity for ammonia synthesis. *J. Am. Chem. Soc.* **138**, 3970–3973 (2016).
- Kimura, H. *Theoretical aspects of band structures and electronic properties of pseudo-one-dimensional solids* **4**, (Springer, 2012).
- Testardi, L. R. Structural instability and superconductivity in A-15 compounds. *Rev. Mod. Phys.* **47**, 637–648 (1975).
- Lv, B. et al. Superconductivity in the Mn₅Si₃-type Zr₅Sb₃ system. *Phys. Rev. B* **88**, 134520 (2013).
- Matthias, B. T., Compton, V. B. & Corenzwit, E. Some new superconducting compounds. *J. Phys. Chem. Solids* **19**, 130–133 (1961).
- Sadagopan, V. & Gatos, H. C. Superconductivity in the close-packed intermediate phases of the V–Ir, Nb–Ir, Nb–Rh, Ta–Rh, Nb–Pt, Ta–Pt, and other related systems. *Phys. Status Solidi* **13**, 423–427 (1966).
- Koch, C. C. & Scarbrough, J. O. Superconductivity in Mo–Re and Nb–Ir *σ* phases. *Phys. Rev. B* **3**, 742–748 (1971).
- Corbett, J. D. Exploratory synthesis: the fascinating and diverse chemistry of polar intermetallic phases. *Inorg. Chem.* **49**, 13–28 (2010).
- Guloy, A. M., Mudring, A.-V. & Corbett, J. D. Nine hexagonal Ca₅Pb₃Z phases in stuffed Mn₅Si₃-Type structures with transition metal interstitial atoms z. problems with classical valence states in possible zintl phases. *Inorg. Chem.* **42**, 6673–6681 (2003).
- Leon-Escamilla, E. A. & Corbett, J. D. Hydrogen stabilization. *J. Alloys Compd.* **265**, 104–114 (1998).
- Horyñ, R., Folcik-Kokot, L. & Iliev, N. On superconductivity in the Nb–Ir–O system. *J. Less Common Met.* **57**, 69–74 (1978).
- Häglund, J., Fernández Guillermet, A., Grimvall, G. & Körling, M. Theory of bonding in transition-metal carbides and nitrides. *Phys. Rev. B* **48**, 11685–11691 (1993).
- Bardeen, J., Cooper, L. N. & Schrieffer, J. R. Theory of superconductivity. *Phys. Rev.* **108**, 1175–1204 (1957).
- McMillan, W. L. Transition temperature of strong-coupled superconductors. *Phys. Rev.* **167**, 331–344 (1968).
- Wang, B. & Ohgushi, K. Superconductivity in anti-post-perovskite vanadium compounds. *Sci. Rep.* **3**, 3381 (2013).
- McCallum, R. W., Woolf, L. D., Shelton, R. N. & Maple, M. B. Low temperature heat capacity of nonmagnetic rare earth molybdenum chalcogenides. *J. Phys. Colloq.* **39**, C6-359–C6-360 (1978).
- Carbotte, J. P. Properties of boson-exchange superconductors. *Rev. Mod. Phys.* **62**, 1027–1157 (1990).
- Nagao, Y., Yamaura, J., Ogusu, H., Okamoto, Y. & Hiroi, Z. Rattling-induced superconductivity in the β -pyrochlore oxides AO₂O₆. *J. Phys. Soc. Jpn.* **78**, 64702 (2009).
- Takayama, T. et al. Strong coupling superconductivity at 8.4 K in an antiperovskite phosphide SrPb₃P. *Phys. Rev. Lett.* **108**, 237001 (2012).
- Ohgushi, K. et al. Superconducting phase at 7.7 K in the Hg₈ReO₃ compound with a hexagonal bronze structure. *Phys. Rev. Lett.* **106**, 17001 (2011).
- Moore, S. H. D., Deakin, L., Ferguson, M. J. & Mar, A. Physical properties and bonding in RE₃TiSb₅ (RE = La, Ce, Pr, Nd, Sm). *Chem. Mater.* **14**, 4867–4873 (2002).
- Larson, A. C. & Von Dreele, R. B. General Structure Analysis System (GSAS). Los Alamos National Laboratory Report LAUR, 86–748 (2000).
- Toby, B. H. EXPGUI, a graphical user interface for GSAS. *J. Appl. Crystallogr.* **34**, 210–213 (2001).
- Perdew, J. P., Burke, K. & Ernzerhof, M. Generalized gradient approximation made simple. *Phys. Rev. Lett.* **77**, 3865–3868 (1996).

45. Kresse, G. & Furthmüller, J. Efficient iterative schemes for ab initio total-energy calculations using a plane-wave basis set. *Phys. Rev. B* **54**, 11169–11186 (1996).



Open Access This article is licensed under a Creative Commons Attribution 4.0 International License, which permits use, sharing, adaptation, distribution and reproduction in any medium or format, as long as you give appropriate credit to the original author(s) and the source, provide a link to the Creative Commons license, and indicate if changes were made. The images or other third party

material in this article are included in the article's Creative Commons license, unless indicated otherwise in a credit line to the material. If material is not included in the article's Creative Commons license and your intended use is not permitted by statutory regulation or exceeds the permitted use, you will need to obtain permission directly from the copyright holder. To view a copy of this license, visit <http://creativecommons.org/licenses/by/4.0/>.

© The Author(s) 2017